

Scale analysis on unstructured grids: Kinetic energy and dissipation power spectra on triangular meshes

Stephan Juricke¹, Marcel Oliver², Sergey Danilov³, Anton Kutsenko², and Kai Bellinghausen³

¹Jacobs University Bremen

²KU Eichstätt-Ingolstadt

³Alfred Wegener Institute for Polar and Marine Research

November 24, 2022

Abstract

Fourier spectra are powerful tools to analyse the scale behavior of turbulent flows. While such spectra are mathematically based on regular periodic data, some state-of-the-art ocean and climate models use unstructured triangular meshes. Observational data is often also available only in an unstructured fashion. In this study, scale analysis specifically for the output of models with triangular meshes is discussed and the representable wavenumbers for Fourier analysis are derived. Aside from using different interpolation methods and oversampling prior to the computation of Fourier spectra, we also consider an alternative scale analysis based on the Walsh–Rademacher basis, i.e. indicator functions. It does not require interpolation and can be extended to general unstructured meshes. A third approach based on smoothing filters which focus on grid scales is also discussed. We compare these methods in the context of kinetic energy and dissipation power of a turbulent channel flow simulated with the sea ice-ocean model FESOM2. One simulation uses a classical viscous closure, another a new backscatter closure. The latter is dissipative on small scales, but anti-dissipative on large scales leading to more realistic flow representation. All three methods clearly highlight the differences between the simulations as concerns the distribution of dissipation power and kinetic energy over scales. However, the analysis based on Fourier transformation is highly sensitive to the interpolation method in case of dissipation power, potentially leading to inaccurate representations of dissipation at different scales. This highlights the necessity to be cautious when choosing a scale analysis method on unstructured grids.

1 **Scale analysis on unstructured grids: Kinetic energy**
2 **and dissipation power spectra on triangular meshes**

3 **S. Juricke^{1,2}, K. Bellinghausen², S. Danilov^{1,2}, A. Kutsenko^{1,3}, M. Oliver^{1,3}**

4 ¹Jacobs University, Department of Mathematics and Logistics, Bremen, Germany

5 ²Alfred Wegener Institute for Polar and Marine Research, Bremerhaven, Germany

6 ³Mathematical Institute for Machine Learning and Data Science, KU Eichstätt–Ingolstadt, Germany

Corresponding author: Stephan Juricke, s.juricke@jacobs-university.de

Abstract

Fourier spectra are powerful tools to analyse the scale behavior of turbulent flows. While such spectra are mathematically based on regular periodic data, some state-of-the-art ocean and climate models use unstructured triangular meshes. Observational data is often also available only in an unstructured fashion. In this study, scale analysis specifically for the output of models with triangular meshes is discussed and the representable wavenumbers for Fourier analysis are derived. Aside from using different interpolation methods and oversampling prior to the computation of Fourier spectra, we also consider an alternative scale analysis based on the Walsh–Rademacher basis, i.e. indicator functions. It does not require interpolation and can be extended to general unstructured meshes. A third approach based on smoothing filters which focus on grid scales is also discussed.

We compare these methods in the context of kinetic energy and dissipation power of a turbulent channel flow simulated with the sea ice-ocean model FESOM2. One simulation uses a classical viscous closure, another a new backscatter closure. The latter is dissipative on small scales, but anti-dissipative on large scales leading to more realistic flow representation. All three methods clearly highlight the differences between the simulations as concerns the distribution of dissipation power and kinetic energy over scales. However, the analysis based on Fourier transformation is highly sensitive to the interpolation method in case of dissipation power, potentially leading to inaccurate representations of dissipation at different scales. This highlights the necessity to be cautious when choosing a scale analysis method on unstructured grids.

Plain Language Summary

To better understand the physical processes that drive and define the circulation in our oceans, it is necessary to analyse the temporal and spatial scales on which these processes act. Classical methods to investigate the spatial scale behaviour is the Fourier analysis which splits any given data into waves of different amplitudes and wavelengths. Mathematically this requires data on an equidistantly spaced grid. However, many ocean models apply triangular or other irregular grids for their computations of oceanic flows. In this study, we describe the advantages and disadvantages of applying Fourier analysis for models that use triangular meshes, with prior interpolation of data to regularly spaced rectangular meshes. We also introduce two other methods that can analyse the distribution of kinetic energy and kinetic energy dissipation across scales without inter-

39 polation. The results show that one needs to be very careful when choosing a specific
40 scale analysis and, potentially, an interpolation method for triangular grids, especially
41 when it comes to analysing the process of kinetic energy dissipation.

42 **1 Introduction**

43 Improving our understanding of scaling laws in geophysical fluid dynamics is of fun-
44 damental importance when analysing crucial scale interactions or, in the context of model
45 development, when designing parameterizations for the unresolved subgrid scales (e.g.
46 Danilov et al., 2019). Scale analysis of turbulent flows is a classical approach to inves-
47 tigate the dynamics simulated by numerical models (e.g. Soufflet et al., 2016; Schubert
48 et al., 2020) and to compare them to observational estimates (e.g. Wang et al., 2019).
49 A variety of methods is available to separate out specific scales in multiscale flows (e.g.
50 Kumar & Foufoula-Georgiou, 1997) or to coarse-grain or filter the information from smaller
51 scales to larger scales (e.g. Aluie et al., 2018; Aluie, 2019; Berloff, 2018; Grooms et al.,
52 2021; Sadek & Aluie, 2018). These methods generally involve spatial or temporal filters
53 to remove specific scales, or projectors which split the data into a hierarchy of Hilbert-
54 subspaces. Such coarse-graining is less straight forward on unstructured triangular meshes,
55 but can nevertheless be designed to achieve conservation of certain quantities or deriva-
56 tives (Patching, 2022).

57 For the distribution of energy over scales in eddy-resolving simulations, a commonly
58 applied scale separation method relying on basis decomposition is Fourier analysis which
59 separates the data into waves of different wavelengths. However, Fourier analysis relies
60 on a set of assumptions that are not always met by model or observational data. Two
61 of the most common discrepancies are the potential lack of regular, equidistant data points
62 in case of unstructured data and the lack of periodicity along boundaries in case of com-
63 plex domains. In this study, we will discuss some of the issues related to Fourier anal-
64 ysis in the context of a model with triangular rather than rectangular spatial discretiza-
65 tion. We will also introduce and discuss the possibility of an alternative analysis that
66 uses the Walsh–Rademacher basis (indicator functions) instead of the Fourier basis which,
67 in many respects, is more suitable for unstructured data.

68 Observational data is often inherently unstructured due to the nature of local mea-
69 surements. When it comes to numerical modelling, on the other hand, some models are

70 also formulated on unstructured triangular meshes and place the degrees of freedom (DoF)
 71 on vertices or triangles. They include, e.g., global-scale models such as FESOM (Danilov
 72 et al., 2017), ICON (Korn, 2017) and coastal models such as FVCOM (Chen et al., 2003),
 73 SCHISM (Zhang et al., 2016), or SUNTANS (Fringer et al., 2006). Concerning Fourier
 74 analysis, the first question that arises for such models is: Which wavenumbers can be
 75 represented on triangular meshes? Relying on well-known facts from solid-state physics
 76 (e.g. Kittel, 2004), one can link the representable wavenumbers to the notion of prim-
 77 itive translation vectors. They define a primitive mesh cell, a reciprocal lattice in wavenum-
 78 ber space, and the smallest resolved wavelengths. On regular triangular meshes the prim-
 79 itive cell is a rhombus consisting of two triangles with opposite orientation. Importantly,
 80 the number of triangles is approximately twice that of the mesh vertices, which creates
 81 an illusion that the DoF placed on triangles resolve larger wavenumbers than the DoF
 82 placed at vertices. It turns out that the increased number of DoF leads to modes of vari-
 83 ability inside of the unit cells of the respective grid (i.e. internal variability modes), leav-
 84 ing the representable wavenumbers without changes.

85 In order to compute Fourier spectra on general (unstructured) meshes, one can-
 86 not rely on a regular placement of the DoF and has to interpolate to a regular quadri-
 87 lateral grid. This leads to some (arbitrary) sampling of original data, which generally
 88 does not create ambiguities for the spectra of variance which are rapidly decaying at large
 89 wavenumbers. However, larger uncertainties may occur for the power spectra of dissipa-
 90 tion (due to horizontal viscosity or diffusion). Such spectra are needed, for example,
 91 to judge on the effective resolution, which is the smallest scale where dynamics are un-
 92 affected by (numerical) dissipation (Soufflet et al., 2016). They are also necessary to in-
 93 tercompare different types of momentum closures. The dissipation power on unstructured
 94 meshes is computed as a dot product between a field and its dissipation tendency which
 95 depends on the numerical operator that parameterizes the small scales in the momen-
 96 tum equation. The dissipation tendency is often noisy and has a large grid scale contri-
 97 bution, generally because the commonly applied harmonic or biharmonic operators em-
 98 phasize large wavenumbers. The placement of DoF on triangles may further emphasize
 99 the grid-scale variability because of the difference in the orientation of computational
 100 stencils for any two adjacent triangles. Interpolation can be further affected by this ge-
 101 ometrical mode in the placement of triangle centers as illustrated in Fig. 1. Computa-
 102 tions are still possible, but require care. This study will both illustrate the difficulties

103 in the computations as well as possible remedies. Alternative methods that avoid inter-
 104 polation will be discussed and compared to the results of traditional Fourier analysis.
 105 They can be seen as an extension to already existing methods such as Aluie et al. (2018);
 106 Grooms et al. (2021) which mostly focus on scale analysis and scale separation for struc-
 107 tured meshes and for scales considerably larger than the grid scale.

108 We ran into issues raised above in our earlier attempt to compute spectra of dis-
 109 sipation power for runs with different momentum closures. Classical, purely viscous clo-
 110 sures such as the Leith parametrization (Leith, 1996) are designed to be entirely dissi-
 111 pative on all scales with an emphasis on small scale dissipation. Energy backscatter pa-
 112 rameterizations introduced by Jansen et al. (2015); Klöwer et al. (2018); Juricke et al.
 113 (2019); Juricke, Danilov, Koldunov, Oliver, and Sidorenko (2020); Juricke, Danilov, Koldunov,
 114 Oliver, Sein, et al. (2020), on the other hand, enable energy injection on large scales but
 115 dissipation on small scales. They still retain an overall dissipative nature when averaged
 116 across all scales. Scale analysis of dissipation power can highlight this scale dependence
 117 of momentum closures and is, therefore, an important diagnostic to investigate the be-
 118 haviour of momentum closures, especially close to the grid scale. However, as illustrated
 119 in this study, one can easily get a substantially distorted result if one is not careful. Prac-
 120 tical illustrations of these issues rely on data obtained with FESOM2 (Danilov et al., 2017)
 121 for the zonally reentrant channel test case of Soufflet et al. (2016) which focuses on the
 122 simulation of mesoscale turbulence and was run with two different momentum closures,
 123 one purely dissipative parametrization (following Leith, 1996) and one kinematic backscat-
 124 ter parametrization (following Juricke, Danilov, Koldunov, Oliver, Sein, et al., 2020).

125 This study is structured as follows. We begin with the Fourier analysis in section
 126 2 which discusses wavenumbers that can be represented on triangular meshes. We will
 127 discuss some of the consequences for the computation of spectra on interpolated regu-
 128 lar grids. In section 2.4 we will provide a short description of an alternative approach
 129 called *resize-and-average* method (R-a-A) that does not rely on the Fourier basis, but
 130 on the Walsh–Rademacher basis instead. A third diagnostic based on applications of smooth-
 131 ing filters is also briefly introduced. Section 3 describes the simulations with the two dif-
 132 ferent momentum closures, i.e. the Leith and kinematic backscatter parametrizations,
 133 for which we will assess kinetic energy and dissipation power spectra. The next section
 134 4 applies the described methods for scale analysis to the aforementioned simulation data

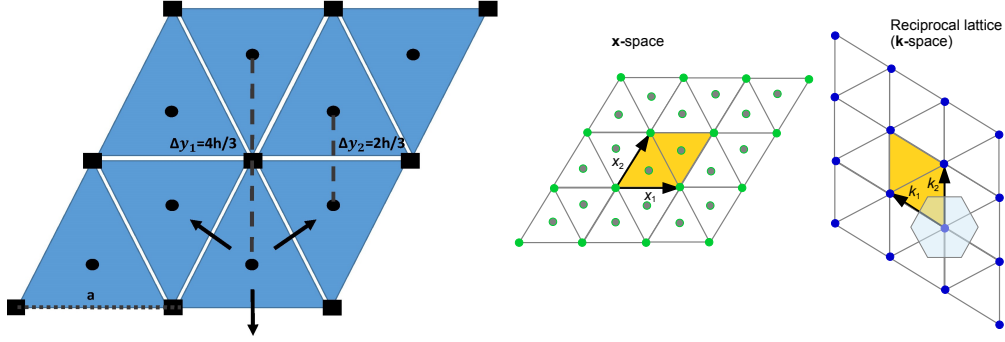


Figure 1. (Left) Regular equilateral triangular mesh with vertices (black squares) and centroids (black circles). There are two types of triangles (pointing upward and downward). The distances between centroids in the y -direction alternate between $2h/3$ and $4h/3$, where h is the height (dashed lines), creating a geometrical pattern in data placed at centroids. The side length of the equilateral triangles is a (dotted line).

(Right) Triangular mesh and its reciprocal lattice in \mathbf{k} -space. Unit cells are shown in orange. The first Brillouin zone is the Voronoi hexagon around an origin point of the reciprocal lattice. Small green and blue circles correspond to $\mathbf{z}_{m,n}$ and $\mathbf{q}_{r,s}$ respectively. Vectors $\mathbf{x}_1, \mathbf{x}_2$ and $\mathbf{k}_1, \mathbf{k}_2$ are defined by mesh geometry, and not by the placement of discrete degrees of freedom.

135 and discusses advantages and disadvantages of the diagnostics. This is followed by dis-
 136 cussion and conclusions in section 5.

137 2 Spectra on triangular meshes

138 2.1 Resolved wave numbers for a regular triangular mesh

Consider an infinite regular triangular mesh composed of equilateral triangles. We introduce coordinates $\mathbf{x} = (x, y)$ with origin at one of the mesh vertices and orient the triangles so that all vertices are obtained from $(0, 0)$ through the set of translations

$$\mathbf{z}_{m,n} = m \mathbf{x}_1 + n \mathbf{x}_2, \quad \mathbf{x}_1 = a(1, 0), \quad \mathbf{x}_2 = a(1/2, \sqrt{3}/2), \quad (1)$$

139 where a is the triangle side length (see also Fig. 1), and m, n are integers. The vectors
 140 \mathbf{x}_1 and \mathbf{x}_2 are referred to as primitive translation vectors. The mesh is invariant to trans-
 141 lation by $\mathbf{z}_{m,n}$. A rhombus, defined by vectors \mathbf{x}_1 and \mathbf{x}_2 , is a primitive unit cell of the
 142 triangular lattice. The selection of vectors \mathbf{x}_1 and \mathbf{x}_2 and the unit cell is not unique. For
 143 example, one can select \mathbf{x}_1 and $\mathbf{x}_2 - \mathbf{x}_1$, and take a rhombus that corresponds to them.
 144 However, all possibilities represent the same group of translations $\mathbf{z}_{m,n}$.

The values of a Fourier harmonic of any scalar or vector field $T = \bar{T} e^{i\mathbf{k}\cdot\mathbf{x}}$, with amplitude \bar{T} and wave vector $\mathbf{k} = (k, l)$, sampled at vertices or centers of like triangles do not change if \mathbf{k} is replaced by $\mathbf{k} + \mathbf{q}$, where \mathbf{q} is such that

$$e^{i\mathbf{q}\cdot\mathbf{z}} = 1. \quad (2)$$

This implies that

$$\mathbf{q} = \mathbf{q}_{r,s} = r \mathbf{k}_1 + s \mathbf{k}_2, \quad (3)$$

where r and s are integers and the vectors \mathbf{k}_1 and \mathbf{k}_2 are such that

$$\mathbf{x}_i \cdot \mathbf{k}_j = 2\pi \delta_{ij}, \quad (4)$$

which gives

$$\mathbf{k}_1 = 2\pi/a (-1, 1/\sqrt{3}), \quad \mathbf{k}_2 = 2\pi/a (0, 2/\sqrt{3}). \quad (5)$$

145 The translations $\mathbf{q}_{r,s}$ define the reciprocal lattice in \mathbf{k} -space (Fig. 1).

146 Because \mathbf{k} can be determined up to the translation $\mathbf{q}_{r,s}$, it is sufficient to consider
 147 only \mathbf{k} -points that are closer to the origin $\mathbf{q}_{0,0}$ than to any other $\mathbf{q}_{r,s}$. These points lie
 148 in the Voronoi polygon obtained by the Voronoi tessellation of the lattice $\{\mathbf{q}_{r,s}\}$ in \mathbf{k} -space.
 149 This hexagon is referred to as the first Brillouin zone and is shown in Fig. 1.

150 The reciprocal lattice and the Brillouin zone are defined by the geometry of the tri-
 151 angular mesh and do not depend on how discrete DoF are placed, unless the DoF and
 152 discretization correspond to a refinement of the given triangular mesh. As a result, one
 153 deals with \mathbf{k} constrained to the first Brillouin zone independent of whether the discrete
 154 DoF are placed on vertices or cells or edges.

The smallest distance from $\mathbf{q}_{0,0}$ to the boundary of the first Brillouin zone is

$$|\mathbf{k}|_{\max} = 2\pi/(\sqrt{3}a) = \pi/h,$$

155 i.e., the *geometric* resolution of the equilateral triangular mesh is defined by the height
 156 of triangles h . This can be compared with $|\mathbf{k}|_{\max} = \pi/a$ for the quadrilateral mesh with
 157 the side a .

158 On triangular meshes there are nearly twice as many cells as vertices. If discrete
 159 DoF are placed on cells, an obvious question is how the increased number of DoF can
 160 be reconciled with the statement that the wave vector is constrained in the same way
 161 to the first Brillouin zone as for the vertex placement. The answer is that the increased

162 number of DoF in this or similar cases creates additional modes of variability inside the
 163 unit cells, as explained, e.g., in Danilov and Kutsenko (2019). The origin of the mode
 164 is related to the difference in the orientation of the stencil of the nearest neighbors. For
 165 a triangle pointing upward in the plane of Fig. 1 the stencil of three nearest neighbors
 166 points downward, and vice versa. Consequently, discrete operators have different rep-
 167 resentation on u and d triangles, and different truncation errors, hence a mode of vari-
 168 ability between the nearest triangles. As a rule, this mode of variability is well controlled
 169 in the existing numerical codes (see, e.g., the discussion of viscous operators in Juricke,
 170 Danilov, Koldunov, Oliver, Sein, et al. (2020) for FESOM), but can contribute to the
 171 apparent grid-scale patterns seen in the dissipation tendency (see section 4.1.2).

172 2.2 Fourier spectra of interpolated fields

173 Triangular meshes used in practice are generally non-uniform. The most common
 174 way to compute spectra in this situation is to interpolate the fields onto a regular quadri-
 175 lateral mesh, then sample and apply the discrete Fourier transform in the standard way.
 176 The theoretical consideration above gives an argument on the resolution of the sampling
 177 mesh (finer than π/k_{\max}). Due to interpolation, some variance can be lost on small scales.

Consider, for definiteness, a scalar discrete field ϕ_c known on mesh cells. When com-
 puting spectra of vector fields, such as kinetic energy spectra, the expressions stated here
 apply component-wise in the respective dot products. We write $c \in \mathcal{T}$ to denote the
 cell index and \mathcal{T} to denote the set of mesh triangles. If ϕ_{mn} is the result of interpola-
 tion of the cell-based ϕ_c to some regular grid, with $1 \leq m \leq M$ and $1 \leq n \leq N$, cov-
 ering the domain of interest, to compute the power spectrum of ϕ , one needs to ensure
 variance preservation in the sense

$$\frac{1}{MN} \sum_{m,n=1}^{M,N} \phi_{mn}^2 \approx \frac{\sum_{c \in \mathcal{T}} \phi_c^2 |A_c|}{\sum_{c \in \mathcal{T}} |A_c|} \quad (6)$$

178 (we assume zero area mean for simplicity). Here, $|A_c|$ denotes the area of cell c .

179 This is easy to achieve if ϕ_c is a primitive variable (velocity, temperature or salin-
 180 ity) with commonly available linear or cubic spline interpolation because such fields are
 181 commonly smooth. They are generally known in a finite-volume sense as mean over the
 182 respective control volumes. The nearest point interpolation method to a sufficiently fine
 183 mesh tends to respect this sense, yet emphasizes discontinuities in interpolated data, which
 184 leads to an artificial spectral pile-up at small scales. Linear and cubic interpolation meth-

185 ods are free from such a drawback, but treat the finite-volume data as point values. Al-
 186 though this is appropriate for smooth fields, it leads to artifacts in the case of spectra
 187 of horizontal dissipation power as discussed later.

To compute dissipation power spectra, one has to interpolate both ϕ_c and the dis-
 sipation tendency, which is either due to the horizontal diffusion or horizontal viscosity,
 apply the Fourier transform to both, and compute their inner product. The dissipation
 tendency on cells will be written as $(L\phi)_c$, where L is a discrete Laplacian operator in
 the simplest case. On regular meshes, one can use a discrete analog the divergence the-
 orem in the form

$$\int_{\Omega} \phi \Delta \phi \, dV = - \int_{\Omega} |\nabla \phi|^2 \, dV + \int_{\partial\Omega} \phi \mathbf{n} \cdot \nabla \phi \, dS, \quad (7)$$

188 where the second integral is over the boundary $\partial\Omega$ of the integration domain Ω and is
 189 negligible if the domain is large enough. As a result, one can compute a power spectrum
 190 of $\nabla \phi$ instead of computing the cross-spectrum. While discrete analogs of similar trans-
 191 formations are maintained on unstructured meshes, they are not always straightforward
 192 (see Juricke et al., 2019, for FESOM operators), and may be not available in model out-
 193 put.

194 In applications, the field ϕ_c is generally smooth while $(L\phi)_c$ often has a noticeable
 195 grid-scale component. Indeed, if the power spectrum of ϕ scales as $k^{-\alpha}$, the envelope of
 196 the Fourier transformed $\phi_{\mathbf{k}}$ scales as $k^{-(\alpha+1)/2}$. The dissipation tendency scales as $k^{-(\alpha+1)/2+2}$
 197 for the harmonic operator L and as $k^{-(\alpha+1)/2+4}$ for the biharmonic one. Thus, when $\alpha =$
 198 3 , the envelope of the Fourier transform of the dissipation tendency is flat even for a har-
 199 monic operator. This amplification of small scales is common to all discretizations, and
 200 explains why the pattern of $L\phi$ can look noisy. For cell-based quantities on triangular
 201 meshes there is one more factor, namely the difference of L on u and d triangles. Here,
 202 the internal degree of freedom is another source of small-scale noise not present in the
 203 case of vertex-based quantities on triangular meshes or in the case of cell-based quan-
 204 tities on quadrilateral meshes.

Because of the grid-scale pattern, even oversampling may fail to ensure that $L\phi$ is
 properly sampled. Writing $(L\phi)_{mn}$ to denote the interpolation of the cell-based quan-
 tity $(L\phi)_c$ to the sampling grid, we need to achieve

$$\frac{1}{MN} \sum_{m,n}^{M,N} \phi_{mn} (L\phi)_{mn} \approx \frac{\sum_{c \in \mathcal{T}} \phi_c (L\phi)_c |A_c|}{\sum_{c \in \mathcal{T}} |A_c|}. \quad (8)$$

205 This approximation is prone to fail, depending on the method of interpolation. For FE-
 206 SOM2, we will show in section 4.1.2 that scale analysis of kinetic energy dissipation is
 207 very sensitive to the specific choice of interpolation onto a regular grid, especially for sim-
 208 ulations that use the backscatter parameterization (Juricke, Danilov, Koldunov, Oliver,
 209 Sein, et al., 2020). For those simulations, dissipation spectral density is negative in the
 210 vicinity of k_{\max} , but can be positive at smaller wavenumbers. The total dissipation power
 211 is negative, but this picture is easily distorted through interpolation. The accuracy in
 212 representing the dissipation power by the interpolated field (such that equation (8) ap-
 213 proximately holds) may serve as a check for the appropriateness of interpolation. Fur-
 214 thermore, angular averaging of two-dimensional spectra, collapsing them to one-dimensional
 215 spectra helps to reduce the side effects of interpolation errors.

216 **2.3 On 1D spectra**

217 1D spectra are a convenient characteristic in test cases that use periodic bound-
 218 ary conditions in one direction (e.g., zonally-reentrant channels). Data are taken along
 219 zonal lines, and no windowing is needed. The spectra computed at different meridional
 220 locations are then averaged. On regular equilateral triangular meshes such lines are drawn
 221 through centroids of u or d triangles. Since the distance between the nearest data point
 222 is a , not all wave numbers are resolved (π/a instead of π/h). Taking data points along
 223 a zigzag line passing through centroids of u and d triangles is potentially resolving higher
 224 wavenumbers, but may create aliasing. If one interpolates to a regular set of points along
 225 a zonal line, the result will depend on the line (and interpolation method). If the line
 226 is drawn through the centers of triangles, only the data at these centers will be used for
 227 linear interpolation. Spectral density at wavenumbers larger than π/a will still be un-
 228 certain.

There is a simple, fundamental reason why especially one-dimensional spectra of
 dissipation are questionable: In the continuous 2D case for $\mathbf{L} = \Delta$,

$$\phi \Delta \phi = \nabla \cdot (\phi \nabla \phi) - |\nabla \phi|^2, \quad (9)$$

229 so that the first (flux divergence) term on the right-hand side does not contribute to 2D
 230 spectra (being the divergence of the product), leading to a negative-definite spectral den-
 231 sity. However, it will always contribute to 1D spectra of dissipation, and may even give

232 a dominant contribution. Averaging of 1D spectra over the other direction will not nec-
 233 essarily fully eliminate this contribution, leading to an unpredictable result.

234 In our experience, meridionally averaged 1D spectra are highly sensitive to the choice
 235 of interpolation method and the location of the interpolation grid, especially for dissi-
 236 pation power spectra which are relatively flat. We found that interpolation such as lin-
 237 ear or cubic may actually lead to considerably distorted line structures on the interpo-
 238 lated grid, depending on the orientation of the triangles. Consequently, the result for cu-
 239 bic and linear interpolation and zonal 1D dissipation power spectra turns out to be fun-
 240 damentally wrong (not shown), as the linear and cubic interpolations smooth out the
 241 small scales and project them onto much large scales in the zonal direction. Even by av-
 242 eraging in the meridional direction, this error is not alleviated and, instead, we produce
 243 spectra that show substantially distorted dissipation powers on large scales. Kinetic en-
 244 ergy spectra, on the other hand, are not much affected by this due to the rapidly de-
 245 caying high wavenumber contribution and can also be computed using 1D spectra av-
 246 eraged in the meridional direction. While we will not discuss one-dimensional line spec-
 247 tra any further, we would like to highlight that these details and consequences need to
 248 be kept in mind when considering 1D spectra on interpolated meshes.

249 **2.4 Scale analysis based on characteristic functions**

250 In this section and section 2.5, we present two alternative approaches to scale anal-
 251 ysis that avoid interpolation and preserve the finite-volume sense in which the data is
 252 represented in the model. The first method is called resize-and-average method (R-a-
 253 A) and we will present it in its original and a modified version. In the following, we de-
 254 scribe the general concept relying on averaging operators on successively smaller sub-
 255 domains of the model domain using the Walsh–Rademacher basis, i.e., a basis generated
 256 by indicator functions of cells of the triangular grid. A detailed mathematical analysis
 257 of this method is provided in Kutsenko et al. (2022).

We identify the data on cells, ϕ_c , with the piecewise-constant function

$$\phi(\mathbf{x}) = \sum_{c \in \mathcal{T}} \phi_c \chi_{A_c}(\mathbf{x}), \quad (10)$$

258 where $\chi_{A_c}(\mathbf{x})$ is the indicator function of mesh cell A_c , so that $\phi(\mathbf{x}) = \phi_c$ for \mathbf{x} within
 259 A_c . Generally, the A_c may be triangles or unions of triangles.

Now consider a submesh \mathcal{S} with elements B_c composed of unions of several neighboring A_c , i.e.,

$$B_c = \bigcup_{c' \in \mathcal{T}_c} A_{c'} \quad (11)$$

for $c \in \mathcal{S}$, where $\mathcal{T} = \cup_{c \in \mathcal{S}} \mathcal{T}_c$ is a partition of the initial mesh. The initial mesh \mathcal{T} generates the Hilbert space

$$L_{\mathcal{T}} = \text{span}\{\chi_{A_c} : c \in \mathcal{T}\}. \quad (12)$$

The coarser sub-mesh generates the Hilbert subspace

$$L_{\mathcal{S}} = \text{span}\{\chi_{B_c} : c \in \mathcal{S}\}. \quad (13)$$

The orthogonal projector onto $L_{\mathcal{S}}$ is given by

$$(\mathbb{P}_{\mathcal{S}}\phi)(\mathbf{x}) = \sum_{c \in \mathcal{S}} |B_c|^{-1} \left(\sum_{c' \in \mathcal{T}_c} \phi_{c'} |A_{c'}| \right) \chi_{B_c}(\mathbf{x}). \quad (14)$$

This gives a decomposition, orthogonal with respect to the standard L^2 inner product

$$\langle \phi, \psi \rangle = \int \phi(\mathbf{x}) \psi(\mathbf{x}) \, d\mathbf{x}, \quad (15)$$

of the space $L_{\mathcal{T}}$ into the coarse subspace $L_{\mathcal{S}}$ with a remainder denoted by $L_{\mathcal{T}/\mathcal{S}}$

$$L_{\mathcal{T}} = L_{\mathcal{S}} \oplus L_{\mathcal{T}/\mathcal{S}}. \quad (16)$$

A field ϕ then decomposes into the orthogonal sum

$$\phi = \mathbb{P}_{\mathcal{T}}\phi = \mathbb{P}_{\mathcal{S}}\phi + \mathbb{P}_{\mathcal{T}/\mathcal{S}}\phi, \quad (17)$$

so that

$$\langle \phi, \psi \rangle = \langle \mathbb{P}_{\mathcal{T}}\phi, \mathbb{P}_{\mathcal{T}}\psi \rangle + \langle \mathbb{P}_{\mathcal{T}/\mathcal{S}}\phi, \mathbb{P}_{\mathcal{T}/\mathcal{S}}\psi \rangle, \quad (18)$$

where the contribution of the remainder subspace is given by

$$\begin{aligned} \langle \mathbb{P}_{\mathcal{T}/\mathcal{S}}\phi, \mathbb{P}_{\mathcal{T}/\mathcal{S}}\psi \rangle &= \langle \phi, \psi \rangle - \langle \mathbb{P}_{\mathcal{T}}\phi, \mathbb{P}_{\mathcal{T}}\psi \rangle \\ &= \sum_{c \in \mathcal{T}} \phi_c \psi_c |A_c| - \sum_{c \in \mathcal{S}} |B_c|^{-1} \left(\sum_{c' \in \mathcal{T}_c} \phi_{c'} |A_{c'}| \right) \left(\sum_{c' \in \mathcal{T}_c} \psi_{c'} |A_{c'}| \right). \end{aligned} \quad (19)$$

260 Through subsequent coarsening, we can construct a hierarchy of subspaces, with the orig-
261 inal mesh \mathcal{T} at the small-scale end going to larger and larger scales.

To compute a spectrum using this construction, we proceed as follows. Consider a sufficiently large square box B^1 with side length L , covering some part of the computational mesh in which the dynamics are sufficiently homogeneous in a statistical sense.

As the coarsest mesh, denoted \mathcal{T}^1 , we take the union of those triangles from \mathcal{T} whose centroids lie inside B^1 . Now introduce a sequence of child bounding boxes obtained by splitting the box B^1 into equal-sized smaller boxes. The smaller boxes will be denoted as $B_{\mathbf{m}}^n$, where the index n indicates that the length of the side of the respective box is L/n , and \mathbf{m} is the shortcut for a pair of indices $\mathbf{m} = (m_x, m_y)$, $1 \leq m_x, m_y \leq n$, describing the position of $B_{\mathbf{m}}^n$ within B^1 . For each child box, we look for a subset $\mathcal{T}_{\mathbf{m}}^n$ of \mathcal{T}^1 including the indices of triangles with centers within $B_{\mathbf{m}}^n$. For every fixed n , $\{\mathcal{T}_{\mathbf{m}}^n\}$ is a partition of \mathcal{T}^1 , and we set

$$\mathcal{T}^n = \bigcup_{\mathbf{m}} \mathcal{T}_{\mathbf{m}}^n. \quad (20)$$

262 We stop at $n = N$ such that all $\mathcal{T}_{\mathbf{m}}^n$ include not more than one triangle. Subsequent
263 refinement will be excessive.

264 When n_1 is a divisor of n_2 , the subspaces associated with \mathcal{T}^{n_1} and \mathcal{T}^{n_2} are orthog-
265 onal so that the norm of the projection to $L_{\mathcal{T}^{n_2}/\mathcal{T}^{n_1}}$ is a measure of the contribution
266 from the scale range $[L/n_1, L/n_2]$ to the total energy.

267 There is some arbitrariness in this construction as the areas occupied by triangles
268 belonging to different $\mathcal{T}_{\mathbf{m}}^n$ are not equal. The relative differences will be small when n
269 is small, but may be large for $n \approx N$. It is possible to get an estimate on the result-
270 ing uncertainty by slightly displacing the box B^1 and repeating computations. The ad-
271 vantage of this method is that it works for structured as well as unstructured meshes.

Here, to obtain a finer separation at smaller scales, we chose $n_1 = n$ and $n_2 = n + 1$, define the scale points

$$\ell_n = \frac{L}{n}, \quad (21)$$

the spectral energy density of the field ϕ ,

$$E(\ell_n) = \langle \mathbb{P}_{\mathcal{T}^n} u - \mathbb{P}_{\mathcal{T}^{n+1}} u, \mathbb{P}_{\mathcal{T}^n} u - \mathbb{P}_{\mathcal{T}^{n+1}} u \rangle, \quad (22)$$

and the spectral dissipation power density

$$E_{\text{dis}}(\ell_n) = \langle \mathbb{P}_{\mathcal{T}^n} u - \mathbb{P}_{\mathcal{T}^{n+1}} u, \mathbb{P}_{\mathcal{T}^n} \mathbf{L}u - \mathbb{P}_{\mathcal{T}^{n+1}} \mathbf{L}u \rangle. \quad (23)$$

272 Fig. 8 shows examples of an energy spectrum $(\ell_n, E(\ell_n))$, left, and a dissipation power
273 spectrum $(\ell_n, E_{\text{dis}}(\ell_n))$, right.

In the orthogonal case, when n_1 divides n_2 ,

$$\langle \mathbb{P}_{\mathcal{T}^{n_2}} u - \mathbb{P}_{\mathcal{T}^{n_1}} u, \mathbb{P}_{\mathcal{T}^{n_2}} u - \mathbb{P}_{\mathcal{T}^{n_1}} u \rangle = \langle \mathbb{P}_{\mathcal{T}^{n_2}} u, \mathbb{P}_{\mathcal{T}^{n_2}} u \rangle - \langle \mathbb{P}_{\mathcal{T}^{n_1}} u, \mathbb{P}_{\mathcal{T}^{n_1}} u \rangle, \quad (24)$$

and

$$\langle \mathbb{P}_{\mathcal{T}^{n_2}} u - \mathbb{P}_{\mathcal{T}^{n_1}} u, \mathbb{P}_{\mathcal{T}^{n_2}} \mathbb{L}u - \mathbb{P}_{\mathcal{T}^{n_1}} \mathbb{L}u \rangle = \langle \mathbb{P}_{\mathcal{T}^{n_2}} u, \mathbb{P}_{\mathcal{T}^{n_2}} \mathbb{L}u \rangle - \langle \mathbb{P}_{\mathcal{T}^{n_1}} u, \mathbb{P}_{\mathcal{T}^{n_1}} \mathbb{L}u \rangle. \quad (25)$$

274 When $n_1 = n$ and $n_2 = n + 1$ and these identities no longer hold, experiments show
 275 that the left-hand expressions in (24) and (25) are less noisy than the respective right-
 276 hand expression, which motivates their choice for the diagnostics (22) and (23). A the-
 277 oretical justification for this choice and a mathematical analysis along the lines of Kutsenko
 278 et al. (2022) of this modified extended version of the R-a-A method is open and a topic
 279 of current research.

280 2.5 Scala analysis via discrete spatial filtering

281 The second method, which is in some respect related to the R-a-A method, is based
 282 on the use of spatial filters. It also has conceptual overlap with, e.g., Sadek and Aluie
 283 (2018); Grooms et al. (2021), but differs in the fact that it uses the natural discrete fil-
 284 ter operation used in FESOM2.

More specifically, we apply several cycles of a smoothing filter that was also used
 by Juricke et al. (2019) and Juricke, Danilov, Koldunov, Oliver, Sein, et al. (2020) to en-
 hance the spatial scale of the backscatter term of their backscatter parametrization. It
 projects via an area weighted average the field under consideration a_c , which is stored
 on cell centroids, first from the cell centroids to the vertices using the operator \mathbb{X}

$$(\mathbb{X}a)_v = \sum_{c \in \mathcal{C}(v)} a_c (|A_c|/3) / \sum_{c \in \mathcal{C}(v)} (|A_c|/3), \quad (26)$$

where $\mathcal{C}(v)$ is the set of cells containing vertex v . After that, the new quantity b_v defined
 on vertices is then averaged back to the centroids using the operator \mathbb{C}

$$(\mathbb{C}b)_c = \frac{1}{3} \sum_{v \in \mathcal{V}(c)} b_v, \quad (27)$$

285 where $\mathcal{V}(c)$ is the set of vertices of cell c (see Juricke, Danilov, Koldunov, Oliver, Sein,
 286 et al., 2020, for more details). In this way, nearest neighbor averaging enhances the scale
 287 of the fields and filters out smaller scales. However, while the combined smoothing fil-
 288 ter $\mathbb{F} = \mathbb{C}\mathbb{X}$ is the same as the one used in the computational design of the viscous clo-
 289 sure and it conserves globally integrated quantities, the smoothed fields are not orthog-
 290 onal to each other, i.e. larger scales are consecutively mixed with each iteration of the
 291 filter. Nevertheless, when one is specifically interested in the grid scale behaviour and

292 differences therein between different momentum closures, this method is quite useful when
 293 only few iterations are applied, as it focuses first on the smallest resolved scales. Fur-
 294 thermore, it allows to investigate the spatial structure of dissipation power for a single
 295 time instance, rather than relying on spatial and temporal averaging as is the case for
 296 Fourier analysis. This method was already used by Juricke, Danilov, Koldunov, Oliver,
 297 Sein, et al. (2020, their Fig. 4 and 5) and we add this diagnostic here for completeness.

298 **3 Data setup**

299 We use data generated by the ocean model FESOM2 in a channel setup described
 300 in Soufflet et al. (2016) with periodic boundaries in the east-west direction and fixed bound-
 301 aries in the North and South. The domain has a zonal length of 500 km and a merid-
 302 ional length of 2000 km. The grid spacing, i.e., the edge length a of a triangular cell, is
 303 20 km. Despite the ability of FESOM2 to locally refine the grid, we employ a regular tri-
 304 angular grid in this study (see Fig. 1) as it corresponds to the idealized setup also used
 305 by Juricke, Danilov, Koldunov, Oliver, Sein, et al. (2020).

306 Following the discussion in section 2, the smallest resolved wavelengths correspond-
 307 ing to wavenumbers π/h and π/a for a maximum channel length of $\sqrt{(500^2 + 2000^2)}$
 308 are approximately 34.64 km and 40 km. However, the highest wavenumber that can be
 309 ideally represented is along a zigzag line in the zonal direction between meridionally slightly
 310 shifted centroids (see Fig. 1). In that case, the centroids are in zonal direction only $a/2$
 311 apart and the corresponding maximum wavenumber and minimal wavelength are $2\pi/a$
 312 and 20 km, respectively. However, as mentioned in section 2, part of the information for
 313 these higher wavenumbers beyond π/h and up to $2\pi/a$ may already be a reflection of
 314 the spectrum from second and higher Brillouin zones and may be part of the internal
 315 mode of variability inside the unit cell, i.e. inside a rhombus consisting of two triangles
 316 of opposite orientation. We nevertheless plot the Fourier spectra up to these high wavenum-
 317 bers in section 4.1 to discuss the behaviour at the grid scale.

318 In the channel simulations, a South-North temperature gradient is reinforced through
 319 relaxation of the mean density profile, with warm temperatures in the South and cooler
 320 temperatures in the North. A mean current runs from West to East and mesoscale tur-
 321 bulence develops in the middle of the channel (see Fig. 2). Simulations with different vis-
 322 cosity closures are available, using classical viscous closures such as Leith (1996), as well

323 as recently developed backscatter closures, following, for example, the kinematic backscat-
 324 ter of Juricke, Danilov, Koldunov, Oliver, Sein, et al. (2020). In this study, we will fo-
 325 cus on these two simulations, i.e. one with a Leith viscosity closure (LEITH) and one
 326 with kinematic backscatter (KBACK). The data was generated in the context of the re-
 327 cent study by Juricke, Danilov, Koldunov, Oliver, Sein, et al. (2020) where a kinematic
 328 backscatter parametrization was introduced – see the detailed discussion therein. We chose
 329 these two simulations as they are expected to behave fundamentally different when it
 330 comes to dissipation power spectra. While LEITH is purely dissipative on all scales (when
 331 taking into account the entire simulation domain), KBACK is expected to anti-dissipate
 332 on large scales and dissipate on small scales. Averaged over all scales, it is still dissipa-
 333 tive. As we intend to investigate the detailed differences in dissipation behavior of var-
 334 ious momentum closures in future studies, these two simulations serve as a testbed to
 335 assess the merits of the different scale analysis methods.

336 Given the data on the triangular grid, we employ several interpolation methods be-
 337 fore computing classical 2D energy spectra. The interpolation methods between the tri-
 338 angular and the rectangular mesh vary in both the chosen interpolation scheme (near-
 339 est neighbor, linear, cubic) and the resolution of the interpolated grid ($0.09^\circ = 10$ km,
 340 $0.045^\circ = 5$ km, $0.01^\circ \approx 1.1$ km). The details of these choices will be discussed in the
 341 results section below. The final spectra are always computed as an average of daily spec-
 342 tra for 9 years of simulation after the initialization year, i.e., we neglect the first year af-
 343 ter initialization from the mean state as the turbulence needs time to develop. To ini-
 344 tiate the development of turbulence, a small perturbation is applied to the originally bal-
 345 anced mean state. Furthermore, in the spectra discussed below, we only show results for
 346 wavenumbers up to the grid resolution of $a = 20$ km. As we substantially oversample
 347 in the case of the interpolation grids with higher resolution, e.g. at $0.01^\circ \approx 1.1$ km, the
 348 highest wavenumbers above a wavelength of the nominal grid resolution of $2h \approx 34.64$ km
 349 partly correspond to a reflection of the spectrum. They contain some of the information
 350 from the resolved spectrum due to the reflection as well as the effects of the interpola-
 351 tion method. However, the even higher wavenumber part of the spectrum (which cor-
 352 responds to oversampling of the interpolated grid) especially for lower wavelengths than
 353 $a = 20$ km does generally not contribute much and is therefore not considered further.

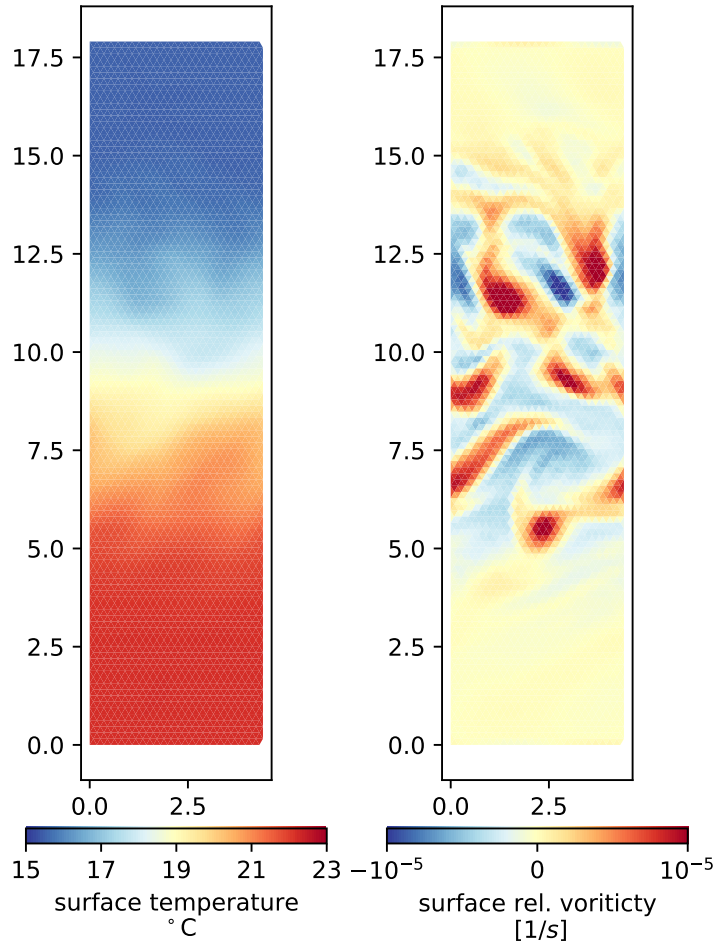


Figure 2. A daily mean of surface (left) temperature [$^{\circ}C$] and (right) relative vorticity [$1/s$] from the LEITH simulation at 20 km resolution, illustrating the eastward flow and enhanced turbulence in the center of the channel.

4 Results

4.1 Fourier scale analysis

We investigate the properties of Fourier spectral analysis obtained via equidistant sampling of interpolated data. Interpolation is done via nearest-neighbor, linear spline interpolation, or cubic spline interpolation. Sampling rates range from 2 times the triangular grid resolution $a = 20$ km (i.e. 10 km) to 18 times the grid scale (i.e. around 1.1 km). Even though the data is not strictly periodic in the meridional direction, turbulence is mostly restricted to the center of the channel and velocities are close to zero near the northern and southern boundaries. We verified that the use of a Hanning win-

363 dow to periodize the data did not change the results; all results shown are computed with-
 364 out windowing.

365 Spectra are shown as a function of inverse wavelength, obtained by summation over
 366 a wave number shell of width one in integer wavenumbers.

367 **4.1.1 Kinetic energy spectra**

368 As a first sanity check to assess the accuracy of the interpolation with respect to
 369 the area-averaged kinetic energy, we compute the ratio between the right and left-hand
 370 side of equation 6, i.e., the ratio of total kinetic energy on the original vs. the interpo-
 371 lated grid. Deviations from 1 correspond to an error in total area-averaged kinetic en-
 372 ergy through interpolation.

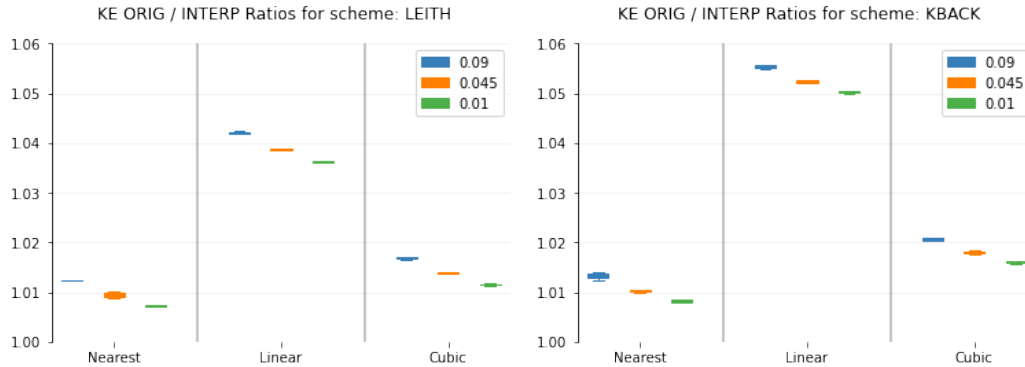


Figure 3. Ratio of average KE averaged for one year on original triangular vs interpolated grid for (left) the LEITH simulation and (right) the KBACK simulation and various interpolation methods and interpolation grid resolutions. The boxes extend from the lower to upper quartile values generated by 9 interpolations with different origins to assess the sensitivity to the horizontal starting point of the interpolation. The upper whiskers end below $Q3 + 1.5(Q3 - Q1)$ and the lower whiskers end above $Q1 - 1.5(Q3 - Q1)$ with $Q3$ and $Q1$ the third and first quartile.

373 We find that the ratio is close to one in all cases (Fig. 3). It is largely independent
 374 of the sampling ratio and only weakly dependent on the method of interpolation, with
 375 nearest-neighbor doing best, and linear interpolation the worst with a maximum error
 376 of around 5.5%. Furthermore, the method seems to be more or less independent from
 377 the choice of simulation, i.e. whether we compute KE spectra for LEITH or KBACK,
 378 with slightly larger values and therefore differences for KBACK (about +0.01, i.e. +1%).

379 Finally, slightly varying offsets of the original starting point for the interpolation (as il-
 380 lustrated by the boxes and whiskers in Fig. 3) only lead to a noticeable variance in the
 381 ratios for the lowest resolution interpolation (i.e. $0.09^\circ = 10$ km).

382 Thus, on this measure, all methods are qualitatively suitable, even though quan-
 383 titative differences already emerge. Whether the deviations from ratio 1 are acceptable
 384 is difficult to say, as the judgement also depends on the scales on which the differences
 385 eventually occur. If only the smallest scales are affected, moderate deviations may still
 386 be reasonable for kinetic energy as the small scales close to the grid scale in a model sim-
 387 ulation are least reliable when it comes to their physical realism.

388 To further assess this question, we turn to actual spectra, choosing the highest over-
 389 oversampling ratio to be on the safe side for representing grid-scale features. First, we ob-
 390 serve that the spectrum for LEITH has overall less KE on all scales when compared to
 391 KBACK (Fig. 4). This is in line with the discussion of Juricke, Danilov, Koldunov, Oliver,
 392 Sein, et al. (2020) who developed kinetic energy backscatter for precisely the reason to
 393 reduce overdissipation and loss of KE in the KBACK simulation. This leads to a lift of
 394 kinetic energy levels especially for small wavenumbers by kinetic energy injection at scales
 395 sufficiently removed from the grid scale.

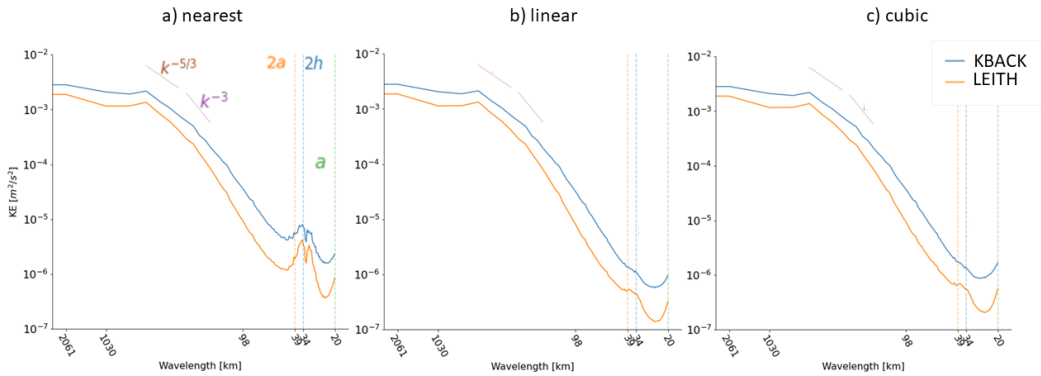


Figure 4. Kinetic energy spectra for simulations with Leith (orange) and kinematic backscatter (blue) momentum closures for (a) nearest neighbor, (b) linear and (c) cubic interpolated data to a 1.1 km grid, averaged for 9 years of simulation.

396 The choice of interpolation methods does not affect the large scales, but leads to
397 substantial differences near the grid scale. This can be explained by the spectral slope
398 of KE in our simulations, with expected power laws of slope between $-5/3$ and -3 . Thus,
399 an interpolation that acts discontinuously on the data, like nearest-neighbor interpola-
400 tion, creates spurious contribution to the energy near the grid scale even though it re-
401 mains closest to the finite-volume interpretation of the data. Continuous or smooth in-
402 terpolation, on the other hand, will not change scaling laws near the grid scale. Conse-
403 quently, linear or cubic interpolation retain the smoothness of the field while still stay-
404 ing close – in an area averaged sense – to the original data. We conclude that especially
405 cubic interpolation is here a sensible choice, as it provides a smooth high wavenumber
406 spectrum as well as a close ratio representation between energy on the original and in-
407 terpolated grid (see Fig. 3).

408 Even though the choice of interpolation method is not critical for KE spectra, it
409 will be crucial for quantities that have steeper or more shallow spectral slope. The shal-
410 low case is the main concern in this paper, and is discussed in detail in section 4.1.2. On
411 the other hand, when computing spectra of quantities that have less variation associated
412 with high wavenumbers, the choice of a smooth interpolation method will be crucial. For
413 example, the spectral slope of sea surface height is, according to theory, between $(-5/3)-$
414 $2 = -11/3$ and $-3 - 2 = -5$ (e.g. Wang et al., 2019). Any roughening of the high
415 wavenumber part of the flow due to the interpolation can show up as a strong peak at
416 high wavenumbers that is emphasized by the logarithmic scaling and the fact that only
417 little variations are associated with small scales, so that relative changes here turn out
418 to be large. The use of nearest-neighbor interpolation would create the impression of a
419 build-up of power close to the cut-off scale of the grid, when they are actually an imprint
420 of the discontinuity of the field in the finite volume representation. Such a build-up may
421 be interpreted as a numerical instability, grid noise or insufficient damping of unrealis-
422 tic small scale grid artifacts rather than an artifact of the interpolation method or the
423 grid discretization itself. Such considerations are especially important if one tries to in-
424 vestigate the effective resolution of a numerical model (see also Soufflet et al., 2016), i.e.,
425 the minimal resolution at which the model still performs reasonably close to reality. One
426 way to define such a minimal resolution is the wavenumber at which the modelled spec-
427 tral slope significantly diverges from the expected theoretical and/or observational slope
428 of an idealized or even global simulation. Therefore, one needs to be careful when inter-

429 preting the high wavenumber end of an interpolated spectrum for data with steep spec-
 430 tral slopes and should be aware of the consequences of the choice of interpolation method.

431 The resolution of the interpolated grid does not change the qualitative picture much.
 432 Using a lower resolution for the interpolation grid does change the high wavenumber rep-
 433 resentation slightly (not shown), but the overall shape of the spectrum and the quali-
 434 tative difference between LEITH and KBACK is not affected. Such a low level sensitiv-
 435 ity to both interpolation method and resolution of interpolation grid suggests a robust
 436 result for the KE spectra. Furthermore, slightly shifting the offset of the interpolation
 437 grid, i.e. varying the position of the first grid point and consequently the entire inter-
 438 polated grid, does also not lead to large changes in the KE spectrum. Only the high wavenum-
 439 bers, which are affected by the interpolation method as well, are also affected by these
 440 slight positional changes of the grid, and the effect is only notable for coarse interpola-
 441 tion grids such as $0.09^\circ = 10 \text{ km}$ (not shown).

442 Finally, the spectra on the oversampled grid exhibit a partial reflection about the
 443 nominal resolution at $2h \approx 34.64 \text{ km}$. This is especially dominant for nearest-neighbor
 444 interpolation where a clear peak occurs at $2h$, after which the spectrum falls off again.
 445 Therefore, a meaningful interpretation of the data is only possible up to a wavelength
 446 of $2h$ as discussed in section 2.

447 ***4.1.2 Dissipation power spectra***

448 Dissipation tendencies emphasize, by design, small scales. Consequently, spectra
 449 of dissipation power – as a product of velocities and dissipation tendencies - are relatively
 450 shallow. Further, dissipation power can be positive or negative. For both of these rea-
 451 sons, dissipation power spectra are displayed on a linear scale.

452 The methodology is very similar to the KE case. We check that the ratio between
 453 the average dissipation power on the triangular grid and the average dissipation power
 454 of the sampled interpolated field is close to 1. Fig. 5 shows that only nearest-neighbor
 455 interpolation passes this test reaching ratios close to 1. All other interpolation schemes
 456 are off by at least 30 % up to as much as a factor of almost 7. In those cases the inter-
 457 polated data is not at all representative of the original data and the results are very sen-
 458 sitive to the viscosity operator used in the respective simulations, with substantially larger
 459 ratios for KBACK.

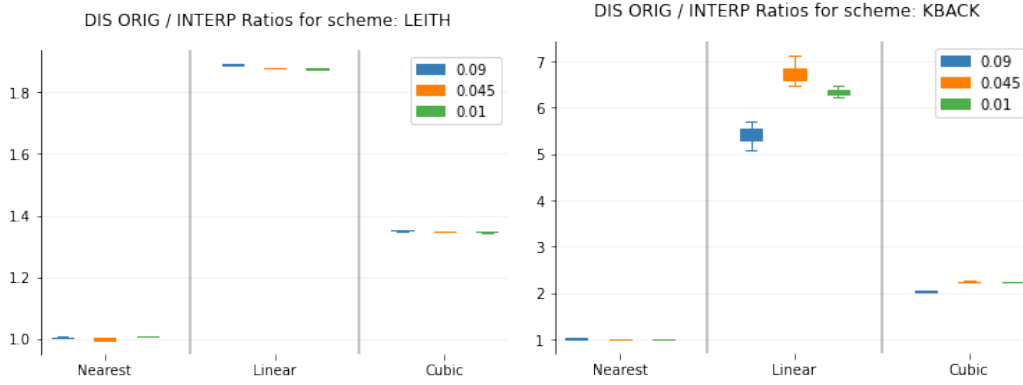


Figure 5. Same as Fig. 3 but for total dissipation power. Note the different y -axis scaling in the left and right panel. For the KBACK simulation with the linear and cubic interpolations, only 95% of the days have been used to compute the ratios. Using 100% of the days would increase the spread between different horizontal starting points even more due to some days where the interpolated results are very close to zero or may even switch sign. Removing 5% of the data does not affect the main interpretation of the results.

460 The reason for this is that the dissipation tendencies used for the computation of
 461 dissipation power have a large grid scale contribution and need to be interpreted in the
 462 discontinuous finite volume sense. In the finite volume model FESOM2 the data is al-
 463 ways associated to a volume or, at a certain vertical level, to a triangular area. Linear
 464 or cubic interpolation, on the other hand, assume that the data is only associated to a
 465 specific point and that a smooth curve exists between two neighboring points, which the
 466 interpolation tries to estimate. This smoothing leads to a loss of information on fine scales
 467 and, as these are important for dissipation tendencies, a loss of information in an over-
 468 all sense. This problem is also not alleviated when moving to finer interpolation reso-
 469 lution, as the conceptual difference in the interpretation of the finite volume data remains
 470 the same.

471 The effect of interpolation is obvious when looking at actual fields (Fig. 6). Inter-
 472 polation smoothes grid scale fluctuations of dissipation power, but emphasizes row-wise
 473 alternating patterns in the meridional direction due to the orientation of the triangles.
 474 This issue persists even at a high oversampling ratio, with patterns that depend strongly
 475 on the orientation and structure of the grid. It explains how small scale fluctuations project
 476 onto large scale structures due to interpolation artifacts. Only nearest-neighbor inter-

477 polation retains grid scale fluctuations in both directions, especially for the dissipation
 478 tendency contribution, as it actually views the data as discontinuous by construction.

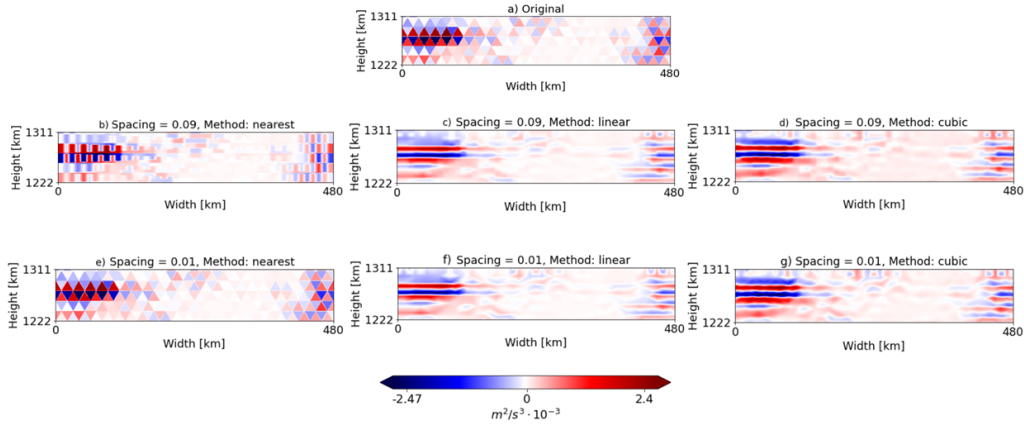


Figure 6. A daily mean of dissipation power for KBACK: a) on the original triangular grid interpreted in the finite volume sense; after interpolation to a $10\text{ km} \times 10\text{ km}$ and $1.1\text{ km} \times 1.1\text{ km}$ grid using nearest neighbor (b and e), linear (c and f) and cubic (d and g) interpolation, respectively. The grid scale structure is only retained by the nearest neighbor interpolation while linear and cubic interpolation lead to smoothing, especially in the zonal direction.

479 Even though linear and cubic interpolation fail even the first sanity check, it is in-
 480 structive to look at actual dissipation power spectra for all three interpolation methods
 481 (Fig. 7). All three methods show that LEITH is dissipative on all scales, while KBACK
 482 dissipates on small scales but injects energy on large scale. For Leith, most of the en-
 483 ergy is dissipated on large scales due to the fact that most of the kinetic energy can be
 484 found at large scales (see Fig. 4) and due to the insufficient scale separation between the
 485 injection and dissipation scales in these simulations at eddy-permitting resolution. The
 486 dissipation operator, while predominantly operating on small scales, is therefore also in-
 487 terfering with the large scales which leads to pronounced dissipation at large scales (see,
 488 e.g., Soufflet et al., 2016; Juricke et al., 2019). However, only nearest-neighbor interpo-
 489 lation is able to show that there is significant dissipation near the grid scale for both LEITH
 490 and KBACK. Worse, linear or cubic interpolated spectra give the impression that the

491 dissipation power in KBACK is predominantly positive, which is physically wrong and
 492 numerically impossible.

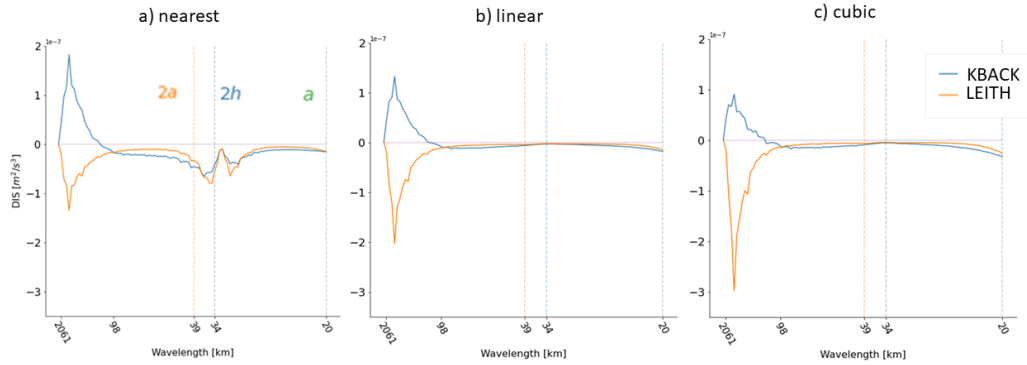


Figure 7. As 4 but for dissipation power spectra.

493 This example illustrates quite nicely, how an inconsistent interpolation of the data
 494 can lead to a quite different and even opposing interpretation of the data. While kinetic
 495 energy is expected to be a physically smooth field, such that cubic or linear interpola-
 496 tion are acceptable choices, dissipation power is, numerically, a discontinuous field and
 497 should be viewed in the finite volume framework of the model discretization.

498 **4.2 Resize-and-average method**

499 The spectra obtained via the R-a-A method are qualitatively similar to the Fourier
 500 spectra (compare Fig. 8 with Fig. 4 and 7). The results show clearly the distribution of
 501 (anti-)dissipation across scales for the backscatter vs. the Leith viscosity and the higher
 502 levels of KE for KBACK.

503 Note that the spectra obtained by Fourier and the modified R-a-A methods are not
 504 directly comparable in terms of exact values for specific scales. For example, on equi-
 505 lateral square meshes of the size 100×100 , if the spectral slope in the Fourier basis is
 506 $-5/3 = -1.66$, then the R-a-A method gives -1.44 . For rectangular or triangular meshes
 507 of different sizes the R-a-A method may further deviate from the results of Fourier anal-

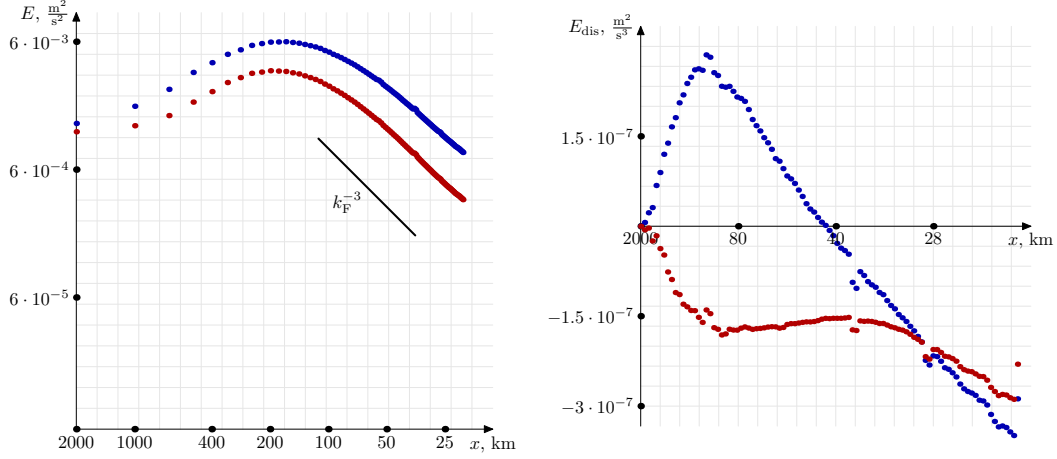


Figure 8. Energy and dissipation power spectra computed by the modified resize-and-average method, see (22) and (23). Blue points correspond to backscatter parametrization, red points to the Leith parametrization.

508 ysis based on interpolated fields. All these aspects are discussed in detail in Kutsenko
 509 et al. (2022), where the exact correspondence between values computed by Fourier and
 510 R-a-A methods is presented. We note that the original R-a-A method determines the
 511 energy density for a specific subset of scales $k \sim 2^n$, $n \in \mathbb{N}$ (see Kutsenko et al., 2022).
 512 The modified R-a-A can recover energy densities for all $k \sim n$. However, the difference
 513 between the slopes in the modified R-a-A and Fourier methods is more noticeable than
 514 in the original R-a-A. For the spectral slope k_F^{-3} in the Fourier basis, the modified R-
 515 a-A gives a two times smaller slope as determined via preliminary idealized tests (not
 516 shown). The theoretical underpinning of the modified R-a-A is a topic of ongoing research.

517 One should refrain from directly comparing the scale diagnostics based on Fourier
 518 and R-a-A analysis. It is more reasonable to compare the results made by the same method
 519 for different simulations. In that case, the qualitative characteristics appearing in spec-
 520 tral diagnostics of LEITH and KBACK are the same for both methods. Another signif-
 521 icant difference between Fourier and R-a-A diagnostics lies in the interpretation of scales
 522 and actual amplitudes. In particular, the resolution x in the original R-a-A method is
 523 about twice smaller than the corresponding wavelength in the Fourier method, as we com-
 524 pare indicator functions with sine and cosine functions. Unsurprisingly, it diverges from
 525 Fourier analysis quantitatively, as it relies on scale averaging rather than trigonometric
 526 separation of the flow.

527 The R-and-A method can be readily applied to any type of unstructured data and
528 does not suffer from the interpolation issue we faced for dissipation power as it always
529 interprets the data in a finite volume sense. But one needs to be aware of the grid res-
530 olution to estimate the maximum resolved wavenumber. Analysing grid scales becomes
531 difficult, as the averaging operation is most effective for subsets with sufficiently many
532 samples inside.

533 4.3 Spectra via discrete spatial filtering

534 We applied the smoothing filter method of section 2.5 specifically to dissipation power
535 to look at the grid scale differences between LEITH and KBACK (Figs. 9 and 10). We
536 first look at the original field and compare it to the local distribution of dissipation power
537 after applying several smoothing filters C and X to see the instantaneous spatial distri-
538 bution of dissipation on larger scales (Fig. 9). While the original field is strongly influ-
539 enced by the grid scale structure of the data, consecutive smoothing cycles reduce the
540 effect of the grid scales and highlight the differential behavior of LEITH compared to
541 KBACK on larger scales. While LEITH remains dissipative on large scales with nega-
542 tive contributions dominating the dissipation power, KBACK switches sign from mostly
543 negative to positive after applying the filters. This illustrates that backscatter tends to
544 dissipate at small scales, while it injects energy at large scales. Furthermore, it demon-
545 strates the sensitivity of overall dissipation to just one single smoothing cycle and, there-
546 fore, the importance to retain small scales when using interpolation for the Fourier anal-
547 ysis. The smoothing filter diagnostic also does not only provide an area averaged pic-
548 ture, but highlights the instantaneous regions of strong dissipation or backscatter.

549 Averaging over the entire model domain for each smoothing cycle and then tak-
550 ing the differences of consecutive smoothing cycles confirms this impression (Fig. 10).
551 While LEITH stays dissipative for all differences, i.e. for all scale ranges, KBACK ac-
552 tually switches from negative to positive already after only one smoothing cycles (Fig. 10).
553 This provides a qualitative illustration of the grid scale behavior of these two methods.
554 However, one can also see that after several smoothing cycles, the dissipation power for
555 both simulations asymptotically tends to zero for large scales. This is due to the fact that
556 the smoothing operation is not orthogonal and therefore does not clearly separate scales.
557 After each iteration of the smoothing filter, more and more large scales are mixed into
558 the small scales and are removed. This is why we can, with the current choice of smooth-

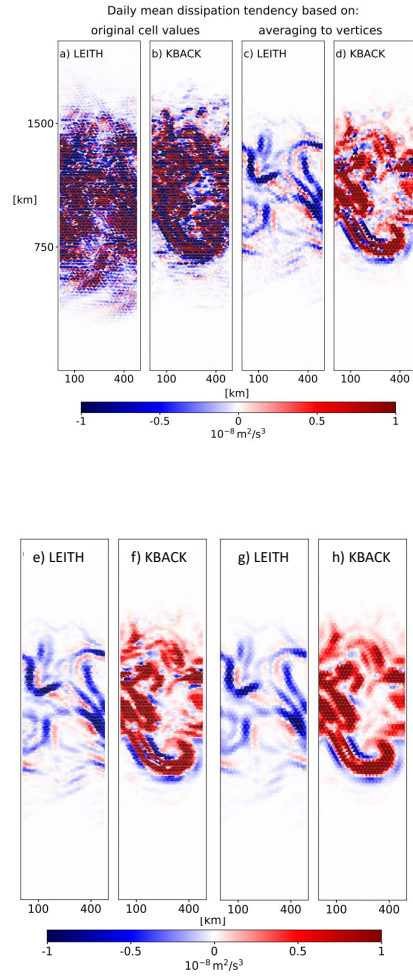


Figure 9. A daily mean of dissipation power on (a+b) the original data, (c+d) after applying the smoothing filter X to velocity and dissipation tendency component before evaluating the scalar product, (e+f) after applying $F = CX$, and (g+h) after applying XCX for (a+c+e+g) LEITH and (b+d+f+h) KBACK.

559 ing filter, only apply the filter method to directly compare two sets of simulations on the
 560 same mesh. Further extension in the spirit of the previous section with the orthogonal
 561 Walsh–Rademacher basis can be developed from here on. However, we want to stress that
 562 the main goal of this specific method is the clear focus on the model grid scale in the con-
 563 text of effective resolution (Soufflet et al., 2016), while the other R-a-A method predom-
 564 inantly focuses on slightly larger up to the largest scales.

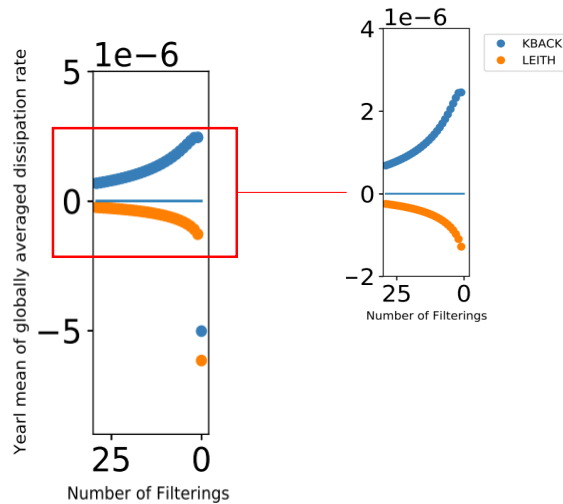


Figure 10. Scale distribution of dissipation power based on globally averaged difference between consecutive smoothing cycles of $F = CX$ (such that data is always placed on centroids) (a) including the original data point without smoothing (i.e. 0 smoothing cycles) and (b) without the original data point.

565 5 Conclusion

566 In this study we investigated several different methods with which to do scale anal-
 567 ysis of kinetic energy and dissipation power on the triangular quasi B-grid of the FE-
 568 SOM2 model. Due to the triangular structure and the placement on centroids, the amount
 569 of velocity points is about twice the amount of scalar points. In the specific idealized struc-
 570 tured triangular grid we consider in this first study, there are two sets of translationally
 571 invariant triangle types, one with upward and one with downward pointing triangles. Con-
 572 sequently, a classical spectral Fourier analysis as a simple 2D spectrum is not fully suf-
 573 ficient. We are effectively dealing with an external mode of variability defined by a rhom-
 574 bus as a unit cell and an internal mode controlled by the two triangles with opposite ori-
 575 entation that make up the rhombus.

576 As alternative pathways to the relatively elaborate full diagnostic of two separate
 577 spectra necessary to describe both modes of variability, we present different methods:
 578 1) a spectral analysis on interpolated fields; 2) an alternative scale analysis based on sub-

579 domain averaging; 3) a small scale analysis based on successive applications of smooth-
580 ing filters.

581 We apply the methods to two sets of data based on a zonally periodic channel for
582 simulations of a primitive equation flow on an equilateral triangular grid with FESOM2.
583 The first data set uses a classical viscous closure. The second one uses a kinematic backscat-
584 ter closure introduced by Juricke, Danilov, Koldunov, Oliver, Sein, et al. (2020).

585 For the first method, i.e. 2D spectral analysis on interpolated fields, one needs to
586 choose both the resolution of the interpolated grid as well as the interpolation method.
587 Oversampling with a finer interpolation grid is necessary to capture the structure of the
588 original triangular grid up its nominal resolution.

589 Regarding the interpolation method, the result is, depending on the investigated
590 field, sensitive to the actual choice. As a first sanity check, one can compute the ratio
591 between the total area-weighted field on the original grid and on the interpolated grid.
592 If these two differ by more than a few percent, the respective interpolation method should
593 not be used. While this first test suggests that all three tested interpolation methods -
594 nearest neighbor, linear and cubic splines - can be used for kinetic energy, only nearest
595 neighbor interpolation should be considered for dissipation power. This is related to the
596 smoothness of the respective fields and the interpretation of the model data. While ki-
597 netic energy should be a physically smooth field, dissipation power is, due to its relation
598 to numerical dissipation tendencies, a very small scale, discontinuous field in the finite
599 volume discretization of FESOM2. Consequently, oversampling via nearest neighbor in-
600 terpolation stays close to the original data. This is also visible in the actual spectra for
601 all three methods. The dissipation power spectra is most sensibly represented by near-
602 est neighbor interpolation, while it leads for linear and cubic interpolation to wrong re-
603 sults for KBACK and LEITH, most noticeable, however, for the data of KBACK. In those
604 simulations, all three methods suggest energy injection at large scales and energy dis-
605 sipation at small scales, as expected. However, only nearest neighbor interpolation shows
606 sufficient dissipation at small scales, while linear and cubic interpolation actually sug-
607 gest too little dissipation at small scales and overall.

608 Looking at kinetic energy spectra, the three different interpolation methods pro-
609 vide very similar results. The kinetic energy backscatter simulation has more energy on
610 all scales compared to the classical viscous closure. Differences between the three inter-

611 polation methods only appear close to the maximum resolved wavenumber. Here, lin-
612 ear and cubic retain a negative slope, while nearest neighbor emphasises the small scales
613 and therefore leads to a small build-up of energy near the grid scale. This build-up is
614 visible due to the small amount of total energy at small scales, so that a small increase
615 in energy at those scales leads to a magnified signal in the spectrum. All three interpo-
616 lation methods provide reasonable spectra, and their difference lies in the interpretation
617 of the data as either a sampling of a naturally smooth field (linear or cubic) or the dis-
618 continuous interpretation of the finite volume discretization (nearest neighbor). Conse-
619 quently, the high wavenumber end of the kinetic energy spectrum should be interpreted
620 with caution.

621 As our second method, the alternative R-a-A scale analysis based on subdomain
622 averaging introduced by Kutsenko et al. (2022) is not directly comparable with Fourier
623 analysis in a quantitative sense. But it reproduces both the general shape of the kinetic
624 energy and the dissipation power spectrum found with the Fourier spectral method on
625 interpolated grids. The big advantage with this averaging method is that it does not de-
626 pend on the regularity of the mesh and can be easily extended to fully unstructured meshes.
627 Such meshes and data will be investigated in more detail in follow-up studies. However,
628 scales and amplitudes are not directly comparable between a Fourier spectrum and the
629 R-a-A scale analysis, as, for example, the scales for R-a-A correspond to scales of at least
630 twice the size in the Fourier analysis. The R-a-A method, however, does not directly al-
631 low to investigate grid scale behaviour with high accuracy, as the elements of each sub-
632 domain become fewer and fewer close to the grid scale.

633 To analyze grid scale behaviour in a local sense and especially for dissipation power,
634 the third and final method presented here utilizes a smoothing operator acting on the
635 grid scale, with successive iterations of the filter removing the contribution from small
636 scales. However, as this operator does not divide the domain into orthogonal subsets (con-
637 trary to the R-a-A method), successive applications of the filter tend to mix scale con-
638 tributions. This does not present a substantial issue, though, if only grid scales are of
639 interest, for which a few smoothing cycles are already sufficient.

640 In general, the methods described and tested in this study tend to complement each
641 other. Due the complex structure of the grid, the violation of translational invariance
642 of the triangular cells and a unit cell being defined by two triangular cells and therefore

643 creating an internal mode of variability, we cannot expect to get a good description of
 644 the scale behavior of the flow with just one diagnostic. We need to rely on the combi-
 645 nation of different diagnostics. As a note of caution, one should be aware that interpo-
 646 lation can lead to inaccurate or simply wrong results for spectra, depending on the fields
 647 under consideration. In follow up studies, we will apply selected methods to both reg-
 648 ular and fully unstructured grids and use them to more closely investigate aspects of dif-
 649 ferent momentum closures and flow simulations.

650 **Acknowledgments**

651 This work is a contribution to projects M3 and S2 of the Collaborative Research
 652 Centre TRR 181 “Energy Transfer in Atmosphere and Ocean” funded by the Deutsche
 653 Forschungsgemeinschaft (DFG, German Research Foundation) under project number 274762653.
 654 The computational resources were supplied by the supercomputing facilities at the Al-
 655 fred Wegener Institute in Bremerhaven.

656 **Data accessibility**

657 The model data is publicly available at the DKRZ cloud [https://swiftbrowser](https://swiftbrowser.dkrz.de/public/dkrz_035d8f6ff058403bb42f8302e6badfbc/Juricke2022Spectra/)
 658 [.dkrz.de/public/dkrz_035d8f6ff058403bb42f8302e6badfbc/Juricke2022Spectra/](https://swiftbrowser.dkrz.de/public/dkrz_035d8f6ff058403bb42f8302e6badfbc/Juricke2022Spectra/).
 659 The latest stable FESOM2 release is available at <https://github.com/FESOM/fesom2>.

660 **References**

- 661 Aluie, H. (2019). Convolutions on the sphere: Commutation with differential op-
 662 erators. *GEM-International Journal on Geomathematics*, *10*. DOI: [https://doi](https://doi.org/10.1007/s13137-019-0123-9)
 663 [.org/10.1007/s13137-019-0123-9](https://doi.org/10.1007/s13137-019-0123-9)
- 664 Aluie, H., Hecht, M., & Vallis, G. K. (2018). Mapping the energy cascade in the
 665 North Atlantic Ocean: The coarse-graining approach. *J. Phys. Oceanogr.*, *48*,
 666 225–244. DOI: <https://doi.org/10.1175/jpo-d-17-0100.1>
- 667 Berloff, P. (2018). Dynamically consistent parameterization of mesoscale eddies. part
 668 iii: Deterministic approach. *Ocean Modelling*, *127*, 1-15. DOI: [https://doi.org/](https://doi.org/10.1016/j.ocemod.2018.04.009)
 669 [10.1016/j.ocemod.2018.04.009](https://doi.org/10.1016/j.ocemod.2018.04.009)
- 670 Chen, C., Liu, H., & Beardsley, R. C. (2003). An unstructured, finite volume, three-
 671 dimensional, primitive equation ocean model: application to coastal ocean and
 672 estuaries. *J. Atmos. Ocean. Tech.*, *20*, 159–186.

- 673 Danilov, S., Juricke, S., Kutsenko, A., & Oliver, M. (2019). Toward consistent sub-
 674 grid momentum closures in ocean models. In C. Eden & A. Iske (Eds.), *Energy*
 675 *Transfers in Atmosphere and Ocean* (pp. 145–192). Springer-Verlag.
- 676 Danilov, S., & Kutsenko, A. (2019). On the geometric origin of spurious waves in
 677 finite-volume discretizations of shallow water equations on triangular meshes.
 678 *J. Comput. Phys.*, *398*, 108891.
- 679 Danilov, S., Sidorenko, D., Wang, Q., & Jung, T. (2017). The Finite-volumeE Sea
 680 ice–Ocean Model (FESOM2). *Geosci. Model Dev.*, *10*, 765–789.
- 681 Fringer, O. B., Gerritsen, M., & Street, R. L. (2006). An unstructured-grid, finite-
 682 volume, nonhydrostatic, parallel coastal ocean simulator. *Ocean Modelling*, *14*,
 683 139–173.
- 684 Grooms, I., Loose, N., Abernathey, R., Steinberg, J. M., Bachman, S. D., Marques,
 685 G., . . . Yankovsky, E. (2021). Diffusion-based smoothers for spatial filtering of
 686 gridded geophysical data. *Journal of Advances in Modeling Earth Systems*, *13*,
 687 e2021MS002552. DOI: <https://doi.org/10.1029/2021MS002552>
- 688 Jansen, M. F., Held, I. M., Adcroft, A. J., & Hallberg, R. (2015). Energy budget-
 689 based backscatter in an eddy permitting primitive equation model. *Ocean*
 690 *Model.*, *94*, 15–26. DOI: [10.1016/j.ocemod.2015.07.015](https://doi.org/10.1016/j.ocemod.2015.07.015)
- 691 Juricke, S., Danilov, S., Koldunov, N., Oliver, M., Sein, D. V., Sidorenko, D., &
 692 Wang, Q. (2020). A kinematic kinetic energy backscatter parametrization:
 693 From implementation to global ocean simulations. *Journal of Advances in*
 694 *Modeling Earth Systems*, *12*, e2020MS002175. DOI: [https://doi.org/10.1029/](https://doi.org/10.1029/2020MS002175)
 695 [2020MS002175](https://doi.org/10.1029/2020MS002175)
- 696 Juricke, S., Danilov, S., Koldunov, N. V., Oliver, M., & Sidorenko, D. (2020). Ocean
 697 kinetic energy backscatter parametrization on unstructured grids: Impact on
 698 global eddy-permitting simulations. *Journal of Advances in Modeling Earth*
 699 *Systems*, *12*, e2019MS001855. DOI: <https://doi.org/10.1029/2019MS001855>
- 700 Juricke, S., Danilov, S., Kutsenko, A., & Oliver, M. (2019). Ocean kinetic
 701 energy backscatter parametrizations on unstructured grids: Impact on
 702 mesoscale turbulence in a channel. *Ocean Modelling*, *138*, 51–67. DOI:
 703 <https://doi.org/10.1016/j.ocemod.2019.03.009>
- 704 Kittel, C. (2004). *Introduction to solid state physics (8 ed.)*. Wiley.
- 705 Klöwer, M., Jansen, M. F., Claus, M., Greatbatch, R. J., & Thomsen, S. (2018).

- 706 Energy budget-based backscatter in a shallow water model of a double gyre
 707 basin. *Ocean Model.*, *132*, 1–11. DOI: 10.1016/j.ocemod.2018.09.006
- 708 Korn, P. (2017). Formulation of an unstructured grid model for global ocean dynam-
 709 ics. *J. Comput. Phys.*, *339*, 525–552.
- 710 Kumar, P., & Foufoula-Georgiou, E. (1997). Wavelet analysis for geophysical appli-
 711 cations. *Rev. Geophys.*, *35*(4), 385–412. DOI: 10.1029/97RG00427
- 712 Kutsenko, A., Danilov, S., Juricke, S., & Oliver, M. (2022). *On the relation between*
 713 *fourier and walsh–rademacher spectra for isotropic random fields.* (preprint)
- 714 Leith, C. E. (1996). Stochastic models of chaotic systems. *Journal of Physics*
 715 *D*, *98*, 481–491. DOI: [https://doi.org/10.1175/15200426\(1998\)015\(0522:](https://doi.org/10.1175/15200426(1998)015(0522:AIMMOM)2.0.CO;2)
 716 [AIMMOM\)2.0.CO;2](https://doi.org/10.1175/15200426(1998)015(0522:AIMMOM)2.0.CO;2)
- 717 Patching, S. (2022). On divergence- and gradient-preserving coarse-graining for finite
 718 volume primitive equation ocean models. *Ocean Modelling*, *170*, 101941. DOI:
 719 <https://doi.org/10.1016/j.ocemod.2021.101941>
- 720 Sadek, M., & Aluie, H. (2018). Extracting the spectrum of a flow by spatial fil-
 721 tering. *Physical Review Fluids*, *3*, 124610. DOI: [https://doi.org/10.1103/](https://doi.org/10.1103/physrevfluids.3.124610)
 722 [physrevfluids.3.124610](https://doi.org/10.1103/physrevfluids.3.124610)
- 723 Schubert, R., Gula, J., Greatbatch, R. J., Baschek, B., & Biastoch, A. (2020). The
 724 submesoscale kinetic energy cascade: Mesoscale absorption of submesoscale
 725 mixed layer eddies and frontal downscale fluxes. *Journal of Physical Oceanog-*
 726 *raphy*, *50*(9), 2573 - 2589. DOI: 10.1175/JPO-D-19-0311.1
- 727 Soufflet, Y., Marchesiello, P., Lemarié, F., Jouanno, J., Capet, X., Debreu, L., &
 728 Benschila, R. (2016). On effective resolution in ocean models. *Ocean Model.*,
 729 *98*, 36–50.
- 730 Wang, S., Qiao, F., Dai, D., & Zhou, X. (2019). Anisotropy of the sea surface height
 731 wavenumber spectrum from altimeter observations. *Scientific Reports*, *9*,
 732 15896. DOI: <https://doi.org/10.1038/s41598-019-52328-w>
- 733 Zhang, Y. J., Ye, F., Stanev, E. V., & Grashorn, S. (2016). Seamless cross-scale
 734 modeling with schism. *Ocean Modelling*, *102*, 64–81. DOI: [https://doi.org/10](https://doi.org/10.1016/j.ocemod.2016.05.002)
 735 [.1016/j.ocemod.2016.05.002](https://doi.org/10.1016/j.ocemod.2016.05.002)